Catal Lett (2012) 142:959–968
DOI 10.1007/s10562-012-0859-4

Structural and Kinetic Study of the Reduction of CuO–CeO_2/Al_2O_3 by Time-Resolved X-ray Diffraction

Vladimir V. Galvita · Hilde Poelman · Geert Rampelberg · Bob De Schutter · Christophe Detavernier · Guy B. Marin

Received: 10 February 2012 / Accepted: 19 June 2012 / Published online: 3 July 2012

Abstract The crystallographic structure of (11 wt.%)CuO–(6 wt.%)CeO_2/γ-Al_2O_3 has been studied and compared with (11 wt.%)CuO/γ-Al_2O_3 under reducing conditions, using time-resolved in situ X-ray diffraction in the temperature range 25–800 °C. In CuO–CeO_2/Al_2O_3, H_2-TPR reduces the CuO phase to Cu, while in C_3H_8-TPR reduction follows a two-step pathway via Cu_2O. A thermal treatment in He also induces reduction for CuO, albeit at higher temperature. In addition to CuO reduction, the CeO_2 promoter in CuO–CeO_2/Al_2O_3 is also partially reduced, without crystallographic transition, regardless of the atmosphere and at similar temperature where reduction of CuO occurs. Supported CuO as in CuO–CeO_2/Al_2O_3 or CuO/Al_2O_3, is more readily reduced by thermal treatment in He than unsupported CuO and Cu_2O. Moreover, the addition of CeO_2 to the CuO–CeO_2/Al_2O_3 catalyst allows for enhanced reducibility of CuO, compared to CuO/Al_2O_3. The CuO phase in CuO–CeO_2/Al_2O_3 is reduced to Cu_2O and partly to Cu at 700 °C and mainly to Cu at 800 °C in He flow. The thermal reduction of CuO–CeO_2/Al_2O_3 requires an apparent activation energy of 216 kJ/mol.

Keywords Structural investigation · Time-resolved in situ XRD · CuO–CeO_2/Al_2O_3 · Hydrogen and propane reduction · Thermal reduction · Supported metal oxides

V. V. Galvita (✉) · H. Poelman · G. B. Marin
Laboratory for Chemical Technology, Ghent University, Krijgslaan 281, S5, 9000 Ghent, Belgium
e-mail: Vladimir.Galvita@UGent.be

G. Rampelberg · B. De Schutter · C. Detavernier
Department of Solid State Sciences, Ghent University, Krijgslaan 281, S1, 9000 Ghent, Belgium

1 Introduction

For the removal of volatile organic compounds (VOC), catalytic total oxidation is often applied. This process has to be performed at high space velocity, requiring a very active catalyst. In addition, catalytic VOC removal is complex because the gas stream generally contains many organic compounds of diverse chemical nature [1, 2]. The catalytic performance of the employed catalyst is one of the important factors determining the effectiveness of this technique. Two groups of catalytic materials are usually employed for complete oxidation of VOCs in air streams: (i) supported or unsupported noble metal catalysts (mainly Pt and Pd), and (ii) transition metal oxide-based catalysts. Although the former usually have higher activities toward oxidation reactions the high costs of noble metals limit their wide-spread application. Transition metal oxides are less active at lower temperatures but have comparable activity at higher temperatures. Among the transition metal oxides, copper oxide is known to be active for combustion. CuO was reported to be as effective as Pt for the total oxidation of n-butanol and methyl mercaptan [3]. Moreover, CuO/Al_2O_3 has shown excellent performance for the combustion of CO, ethyl acetate, ethanol, propane and toluene [4–6].

The catalytic properties of copper oxide-based catalysts are enhanced by the addition of ceria. Ceria as a promoter for supported copper oxide has shown to present several functions: (a) ceria stabilizes the dispersion of the active component; (b) metal/ceria interactions strongly affect their redox properties and, as a consequence, their catalytic properties; (c) ceria also acts as an oxygen storing component due to the presence of mixed oxidation states (3+/4+) of cerium; (d) inversely, copper interaction with CeO_2 can improve the oxygen storage capacity, diffusivity and

redox properties of the latter by the formation of structural defects. Higher concentrations of oxygen vacancies in the catalyst can enhance catalytic activity, by providing activation sites for di-oxygen.

The mechanism of the oxidation of VOCs over transition metal oxide catalysts, was established to follow Mars and Van Krevelen type redox cycles [6–11]. This mechanism includes two steps: the first step consists of the reactant oxidation using the catalyst lattice oxygen which will be replaced, in the second step by gaseous di-oxygen. It was previously shown that $CuO–CeO_2/Al_2O_3$ catalyst reduction is fully reversible, as the Cu^{2+} state is recovered after a reduction–oxidation cycle. At the same time, re-oxidation of the catalyst is two orders of magnitude faster than its reduction [7]. The catalyst activity for total oxidation is determined by weakly bound oxygen forms i.e. oxygen atoms connected to the oxide surface with a low binding energy, in contrast with the regular lattice oxygen atoms which are more firmly bound [7, 12, 13]. However, adsorbed oxygen species are also reported to participate in the reaction. These two types of weakly bound oxygen species, namely adsorbed oxygen species acting as electrophilic oxygen and lattice "nucleophilic" oxygen, are highly reactive and mainly found over a fully oxidized catalyst [7, 12, 13]. They appear at the surface as the result of equilibrium between the oxide lattice and the gas phase [14]. This equilibrium is dynamic, in that the rate of dissociation of the oxide lattice and evolution of oxygen in the form of di-oxygen is equal to the rate of its incorporation from the gas phase into the lattice.

$$2O^{2-}_{latt} \leftrightarrow 2O^{-}_{2ads} \leftrightarrow O^{-}_{2ads} \leftrightarrow O_{2ads} \leftrightarrow O_{2gas}$$

In the process of oxide lattice dissociation, the oxide ions must be extracted from the surface, electrons injected into the solid, oxygen atoms must recombine to form molecules, which finally desorb as di-oxygen. The reverse series of elementary steps takes place upon incorporation. In this equilibrium situation, the surface is always covered by different oxygen species which are very reactive and available for reaction. The surface coverage by these species depends on the oxygen pressure in the gas phase and the dissociation pressure of the oxide.

As part of the Mars-van Krevelen mechanism, the reduction of the catalyst is often the rate-determining step in the total oxidation process. It was previously shown that reduction of a $CuO–CeO_2/Al_2O_3$ catalyst by propane requires an apparent activation energy of 70 kJ/mol, which is equal to its apparent activation energy determined under total oxidation reaction conditions [7]. Thus, the separate study of the kinetics of catalyst reduction and how this is influenced by the support material is worthwhile in order to establish the parameters determining the reduction. The latter can involve both reduction under gas atmosphere, such as propane as model VOC or hydrogen, as well as thermal reduction as a process which generates weakly bound oxygen on the catalyst surface. Indeed, it was shown previously that Cu^{2+} supported on ZSM-5 can be reduced to Cu^{+} thermally, i.e. without a reductant gas such as H_2 or CO, but purely in vacuo or under an inert gas flow at high temperature [15–18]. Likewise, isolated Cu^{2+} monomers are easily reduced when supported on Al_2O_3 and ZSM-5. On the other hand, less dispersed Cu^{2+} species cannot be perfectly reduced to Cu^{+} ions in vacuo at 700 °C [16]. The loss of oxygen atoms of a $CuO–CeO_2/Al_2O_3$ catalyst due to thermal reduction was also observed during total oxidation of propane or toluene in a temporal analysis of products (TAP) reactor [12, 19].

The effect of the support material and the kinetics of reduction of supported CuO have not been fully clarified. In the present work, we report on the structural and kinetic analysis of the reduction of $CuO–CeO_2/Al_2O_3$, CuO/Al_2O_3 and bulk CuO and Cu_2O in C_3H_8, H_2 and He flow by means of time-resolved in situ X-ray diffraction. The elucidation of the above issues will aid in better understanding the mechanism of oxidation reactions by these oxides.

2 Experiment

2.1 Materials

The (11 wt.%)CuO–(6 wt.%)CeO_2/γ-Al_2O_3 is a commercial mixed metal oxide catalyst, prepared by impregnation of γ-Al_2O_3 with $Cu(NO_3)_2$ and $Ce(NO_3)_4$ precursors. The (11 wt.%)CuO/γ-Al_2O_3 catalyst was synthesized via incipient wetness impregnation of γ-Al_2O_3 with $Cu(NO_3)_2 \cdot 2.5H_2O$ (Sigma-Aldrich), followed by drying at 80 °C for 8 h and calcination above 700 °C for 8 h in air. After grinding, fine powder of grain size 75–100 μm was used for catalyst characterization. The CuO crystallite size in both samples amounts to 100 nm, while the alumina is nano-sized (4 nm crystallites). As reference material, CuO and Cu_2O powders (Sigma-Aldrich) were used, having a crystallite size of $\sim$25 nm.

The bulk chemical composition of the tested catalysts was determined by means of inductively coupled plasma atomic emission spectrometry (ICP-AES) (IRIS Advantage system, Thermo Jarrell Ash). N_2 physisorption at −200 °C was applied to determine the BET specific surface area using a Gemini V (Micromeritics) automated device. A BET surface area for $CuO–CeO_2/\gamma$-Al_2O_3 and CuO/γ-Al_2O_3 of 170 m^2/g was obtained by regression of the experimental data in the range $0.05 < p/p^0 < 0.30$ with the linear BET equation. The largest contribution to this value is from the small sized alumina support. For the

unsupported CuO and Cu_2O, the surface area amounts to 40 m^2/g.

In order to visualise the catalyst particles, high-resolution transmission electron microscopy (HRTEM) images of the supported catalysts were recorded with a JEM-2200FS instrument (JEOL, 200 keV with STEM scanning unit and EDX; probe size 1.5 nm).

2.2 XRD Analysis of the Crystal Phase

Crystallographic analyses for the tested catalysts were performed by means of in situ X-ray diffraction (XRD) measurements in θ–2θ mode using a Bruker-AXS D8 Discover apparatus with Cu-Kα radiation of wavelength 0.154 nm and a linear Vantec detector covering a range of 20° in 2θ. The 1450 detector channels are binned per 8 channels, resulting in an angular resolution of $\sim$0.12°. While the minimal capturing time is 0.1 s, a collection time of typically 10–12 s is used during these experiments.

The effect of reduction on the catalyst structure was investigated by in situ XRD in a flowing gas stream from room temperature to 800 °C. The high temperature experiments were carried out using a home-built reactor chamber with Kapton foil window for X-ray transmission. A 10 mg sample was evenly spread in a shallow groove of a single crystal Si wafer. Interaction of the catalyst material with the Si holder was never observed. The chamber atmosphere was pumped and flushed with a rotation pump (base pressure $\sim 4 \times 10^{-2}$ mbar) before introducing the reducing gas flow. The reduction properties of the catalysts were followed by means of XRD during temperature-programmed reduction (TPR) under reducing (5 vol.% C_3H_8/He or 5 vol.% H_2/He) or inert atmosphere (He). The sample was heated from room temperature to 800 °C at a heating rate of 20 °C/min. On the other hand, isothermal reduction experiments were carried out at temperatures 700, 750 and 800 °C, each time with fresh catalyst material. These preset temperatures were reached by fast heating (rate of 300 °C/min) and then held for 30 min. XRD patterns were recorded throughout the whole isothermal reduction procedure. Finally, programmed stepwise reduction in He was performed over all samples with heating rate 60 °C/min and 10 min dwell time at 400, 600 and 800 °C. All temperatures were measured with a K-type thermocouple and corrected afterwards to a calibration curve of the heating device, which is based on the eutectic systems Au–Si, Al–Si and Ag–Si.

The in situ XRD data were processed using home-built analysis software written in python. The software is based on the scientific libraries *numpy* and *scipy* [20] and [21]. Integrated intensity plots were calculated by summing all XRD intensity in a certain 2θ range at each separate temperature. Averaging of the integrated intensity is performed by convolution with a Gaussian. Peak positions are determined as the mean of a Gaussian, fitted to a XRD peak in a chosen range of 2θ around the peak of interest.

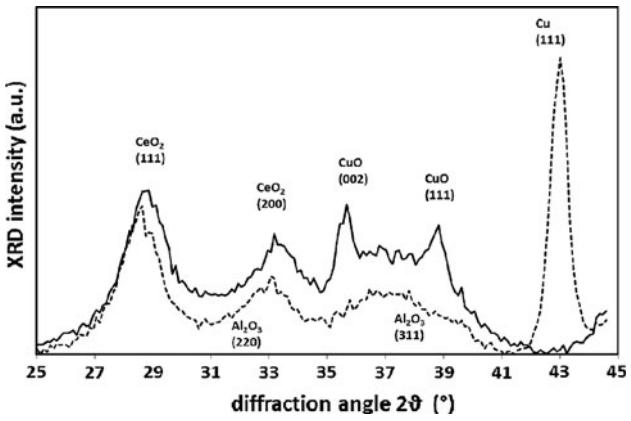

Fig. 1 XRD measurement of $CuO–CeO_2/Al_2O_3$ in oxidized (*solid line*) and reduced state *dashed line*

3 Results and Discussion

Figure 1 shows the XRD patterns for as received and reduced $CuO–CeO_2/Al_2O_3$. Al_2O_3 and CeO_2 present broad diffraction peaks, originating from $\sim$5 nm nano-crystallites. In oxidized state, the catalyst has a CuO phase with sharp diffractions corresponding to crystallites of size $\sim$100 nm. In reduced state, all CuO has turned into a Cu phase with equally sharp diffraction peaks. The crystallographic structure derived from the XRD pattern was confirmed by TEM with line scan EDX of $CuO–CeO_2/Al_2O_3$. Figure 2 shows large CuO single crystal particles and clustered ceria crystallites with copper presence, both embedded in the alumina matrix.

3.1 In Situ XRD During H_2- and C_3H_8-TPR

Figure 3 displays time-resolved XRD data for the TPR of $CuO–CeO_2/Al_2O_3$ catalyst at 20 °C/min heating rate under 5 % H_2/He. Figure 3a displays the intensity of all XRD patterns as function of temperature, while in Fig. 3b a two-dimensional top view of this experiment is presented. Figure 3c displays the diffraction pattern at selected temperatures as indicated in Fig. 3b. The low-temperature patterns shows characteristic lines for CuO at 35.5° (002) and 38.7° (111) (Fig. 3c). No change is seen in the diffraction pattern at temperatures below 250 °C. Beyond this temperature, lines for metallic copper start to appear with the main (111) peak at 43.2°, while the CuO lines disappear (Fig. 3b, c). A separate H_2-TPR at 10 °C/min with on line MS gas analysis showed hydrogen consumption at 177 and 200 °C [6], i.e. shortly before the XRD reduction appears.

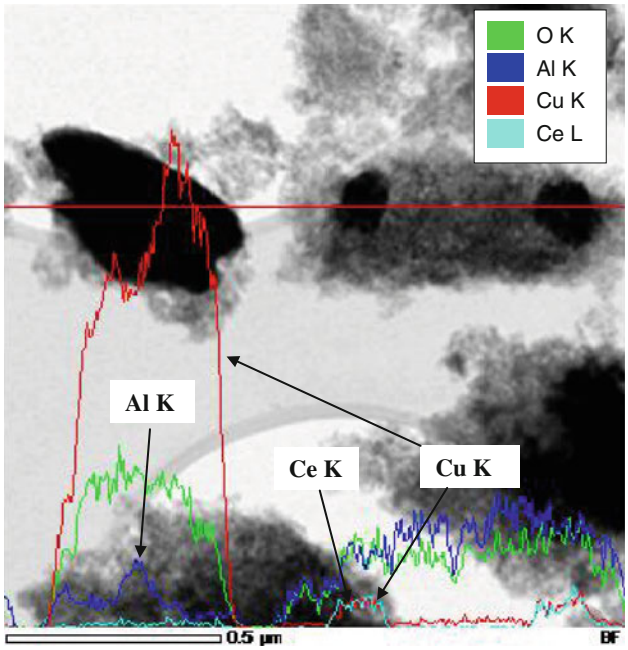

Fig. 2 EDX line scan through a STEM frame on the CuO–CeO_2/γ-Al_2O_3 catalyst, through a CuO particle (*left*) and through two CeO_2 clusters (*middle* and *right*); embedding alumina matrix; probe size 1.5 nm

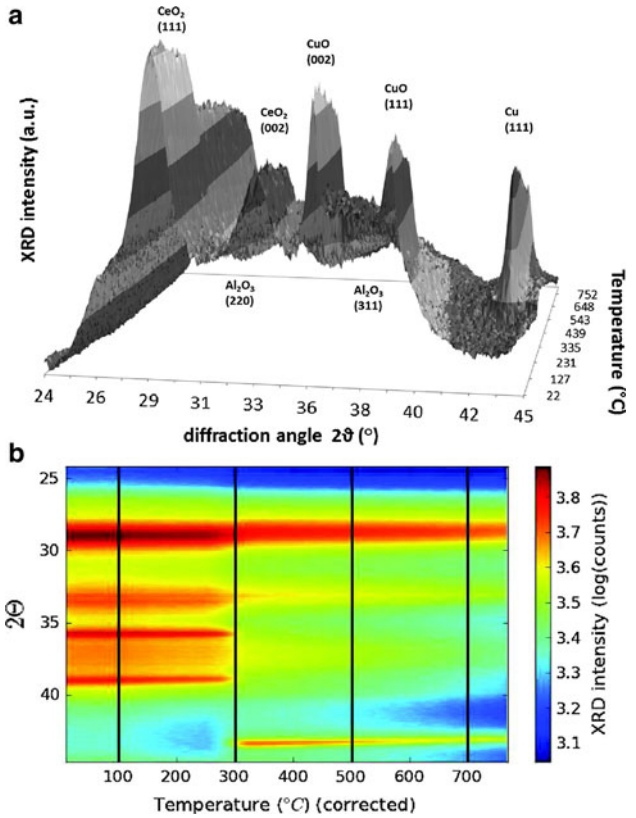

Fig. 3 In situ XRD measurement of CuO–CeO_2/Al_2O_3 during H_2-TPR; **a** 3D variation of XRD intensity as function of calibrated temperature, **b** 2D top view of, **a** *black lines* indicate selected temperatures, **c** XRD pattern at selected temperatures, as indicated in (**b**)

It is clear that during the H_2 reduction of the CuO–CeO_2–Al_2O_3 catalyst, there is no Cu_2O formation [22]. The whole CuO phase is transformed to Cu within a short temperature window around 300 °C, suggesting a direct reduction path:

$$CuO + H_2 \rightarrow Cu + H_2O \quad (1)$$

The absence of an intermediate Cu_2O phase has been reported before [23]. For unsupported CuO, the reduction pathway strongly depends on the TPR conditions used. Kim et al. [24] found that slow heating rates of CuO powder induced a direct reduction, while for faster heating an intermediate Cu_2O phase appeared. Large particles of CuO supported on ZSM-5 equally displayed a direct transition in H_2-TPR, whereas small particles did show an intermediate Cu_2O phase [25]. For H_2 reduction of CuO supported on ZnO or ZrO_2, the presence of an intermediate Cu_2O phase was established in XANES experiments [26, 27]. Similarly, XANES data taken during a H_2 reduction experiment of CuO/SiO_2 indicate that Cu_2O is formed and reduction of copper oxide goes as a sequential reduction [28]:

$$2CuO + H_2 \rightarrow Cu_2O + H_2O \quad (2)$$

$$Cu_2O + H_2 \rightarrow 2Cu + H_2O \quad (3)$$

Whether CuO follows a direct (11) or two-step (2–3) reduction path obviously depends on the conditions of reduction, the CuO particle size and on the nature of the support. For the present catalyst, the main part of the CuO phase is present as large monocrystals of $\sim$100 nm size [29] which puts their direct reduction in line with the CuO particles on ZSM-5 [25].

Characteristic peaks $2\theta = 28.6°$ and 33.1° for the (111) and (200) planes, associated with crystalline CeO_2, appear in the patterns of fresh and H_2 reduced CuO–CeO_2/Al_2O_3 samples. Peaks of the reduced hexagonal phase Ce_2O_3 or of $CeAlO_3$ are never observed. From the XRD measurement, the peak position of the CeO_2(111) peak is determined as a function of temperature (Fig. 4). From the start of the TPR experiment, the angular position of the (111) diffraction is slightly shifting downward, consistent with thermal expansion. Around 257 °C however, an abrupt drop in position occurs, followed by again a more steady shift. A comparative H_2-TPR experiment on pure CeO_2 powder, doesn't show this sudden change in CeO_2(111) position, but rather presents a smooth decrease, consistent with lattice expansion without reaction/reduction. Indeed, unsupported CeO_2 is known to reduce only at higher temperature, namely 500 and 830 °C for high surface area powder and only around 830 °C for low surface area material [30].

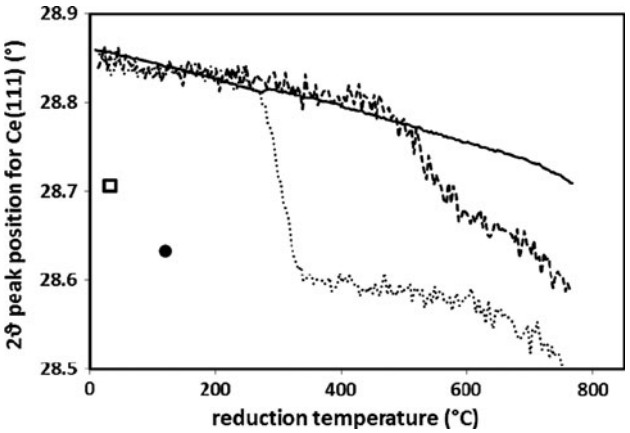

Fig. 4 CeO_2(111) peak position as function of temperature determined from in situ XRD experiment during H_2-TPR for samples CeO_2 (*solid line*) and CuO–CeO_2/Al_2O_3 (*dotted line*), and during and C_3H_8-TPR for CuO–CeO_2/Al_2O_3 (*dashed line*). The single points indicate the value of the peak position after cool down under reducing atmosphere, *open square* after C_3H_8-TPR, *filled circle* after H_2-TPR

The sudden downward change in CeO_2(111) peak position for CuO–CeO_2/Al_2O_3 can be related to a reduction of the CeO_2 phase, which loses lattice O by reacting with hydrogen. Since Ce^{3+} ions occupy more space than Ce^{4+} [31], the reduction results in a lattice size increase, reflected here in a downward shift of the peak position. The reduction of CeO_2 remains partial, as the lower oxide phase Ce_2O_3 is never detected, and it occurs more or less at the same temperature as where CuO is reduced to Cu (300 °C, see Fig. 3). Such a reduction of the CeO_2 promoter phase in parallel to the CuO active phase reduction has been observed previously by means of *operando* XAS experiments following reduction under C_3H_8 and H_2 [29]. Upon cooling down after the reduction experiment, but still under H_2 atmosphere, the peak position only partially returns towards its original value, reflecting the thermal shrinking of the lattice (see Fig. 4).

Figure 5 shows time-resolved XRD data and selected XRD patterns for the C_3H_8-TPR of the CuO–CeO_2/Al_2O_3 (Fig. 5a, b) and CuO/Al_2O_3 (Fig. 5c, d) catalysts at a heating rate of 20 °C/min from room temperature to 767 °C under a 5 % C_3H_8/He mixture. For CuO–CeO_2/Al_2O_3, no changes are seen in the CuO diffraction patterns at temperatures below 400 °C. In contrast to the reduction of CuO–CeO_2/Al_2O_3 by H_2, a Cu_2O phase now appears between 400 and 650 °C, so the transition from Cu^{2+} to Cu^0 occurs through a transient Cu^+ phase. The metal Cu^0 phase starts appearing at a slightly higher temperature of 427 °C. The maximum amount of Cu^+ is observed at temperature 512 °C. At 650 °C, Cu_2O has disappeared and all copper is in metal phase. Overall, these results indicate that CuO in CuO–CeO_2/Al_2O_3 is reduced in a two-step process, i.e. $Cu^{2+} \rightarrow Cu^{+} \rightarrow Cu^0$, by reaction with C_3H_8. The latter is in line with an isothermal in situ XAS study of this catalyst at 350 °C under C_3H_8/He flow [29], which showed reduction of Cu^{2+} through the intermediate Cu^+. As for CuO/Al_2O_3, C_3H_8-TPR equally gives rise to a two-step reduction. The appearance of Cu^+ occurs at similar temperature as for CuO–CeO_2/Al_2O_3 and quickly gives way to Cu^0. C_3H_8-TPR at 10 °C/min with on line MS gas analysis yielded only CO_2 and water. No partial oxidation products were found. The temperatures at which propane consumption occurred, were 325 and 400 °C and a shoulder around 450 °C for CuO–CeO_2/Al_2O_3, and 380 and 440 °C for CuO/Al_2O_3 [6]. As a higher heating rate will shift these values upward, they come close to where reduction starts.

When plotting the CeO_2(111) position for CuO–CeO_2/Al_2O_3 as a function of temperature, again an abrupt shift is noticed, but this time starting around 447 °C compared to 257 °C for H_2-TPR (Fig. 4). So, the CeO_2 promoter is also reduced by C_3H_8 and this at temperatures in the range of Cu^+ formation.

The different reduction behavior of CuO–CeO_2/Al_2O_3 under H_2 and C_3H_8 atmosphere can be due to a different reduction pathway: direct CuO to Cu reduction in H_2, a two-step transition CuO–Cu_2O–Cu with C_3H_8 [22]. Whether or not an intermediate phase appears could equally be related to a different rate of Cu_2O reduction by H_2 and C_3H_8. If under hydrogen, CuO is first reduced to Cu_2O, but this immediately reacts further to form Cu, the formation of a Cu_2O crystallographic phase will never reach long-range order, required for yielding diffraction features in an XRD pattern. With C_3H_8, the reduction rate for Cu_2O is clearly lower, so that Cu_2O can accumulate and as such be observed more easily as a distinct phase.

3.2 In Situ XRD During Thermal Reduction

Vacuum and/or inert atmosphere at high temperature can reduce metal oxides including copper oxide [18, 32]. The overall equation for reduction of CuO is:

$$CuO \leftrightarrow Cu + 0.5O_2 \quad (4)$$

According to the Ellingham diagram, the equilibrium O_2 partial pressure for CuO and Cu_2O at 800 °C is 10^{-4} bar. Hence, from a thermochemical viewpoint copper oxides are unstable under very low pressures of O_2 and at high temperature.

Figure 6 shows time-resolved XRD data for the thermal reduction of the CuO–CeO_2/Al_2O_3 catalyst at 15 °C/min heating rate under He flow. No change is seen in the diffraction pattern at temperatures below 727 °C, after which the dissociation of CuO to Cu_2O starts, reflected in a growing main (111) peak at 36.4°. The faint intensity that arises around 42° from T = 750 °C on, also originates

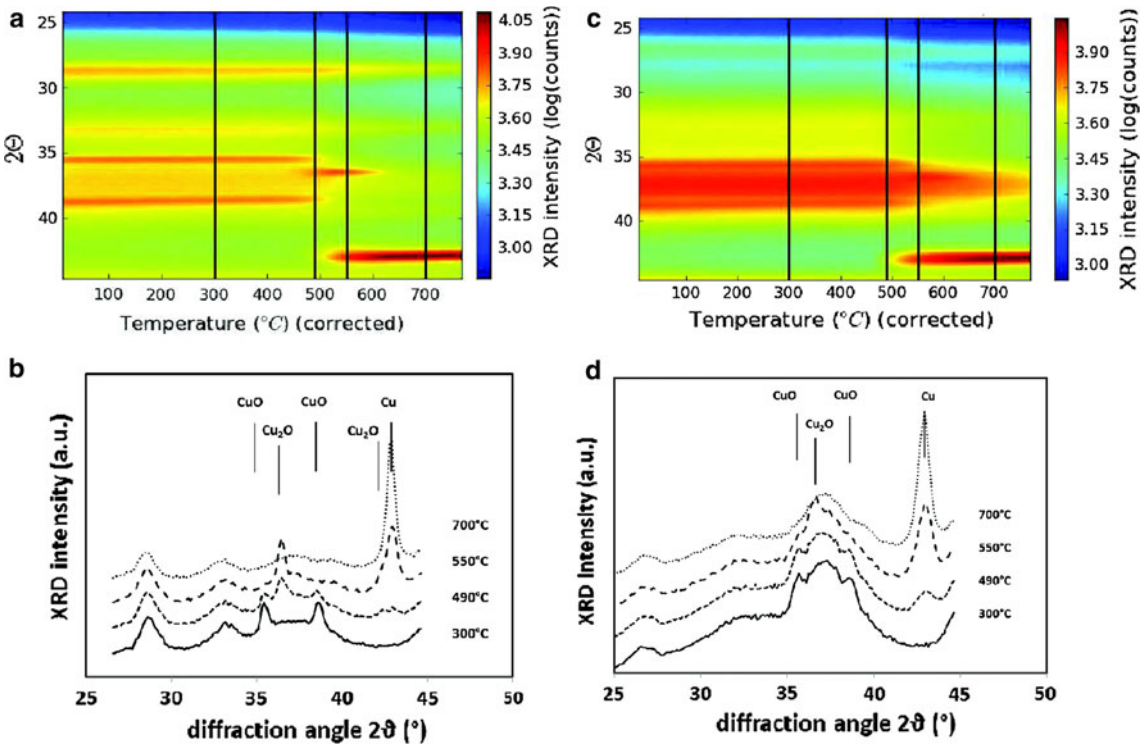

Fig. 5 In situ XRD measurement over $CuO–CeO_2/Al_2O_3$ (**a**, **b**) and CuO/Al_2O_3 (**c**, **d**) during C_3H_8-TPR; **a**, **c** 2D variation of XRD intensities with calibrated temperature, *black lines*: selected temperatures; b, d XRD pattern at selected temperatures

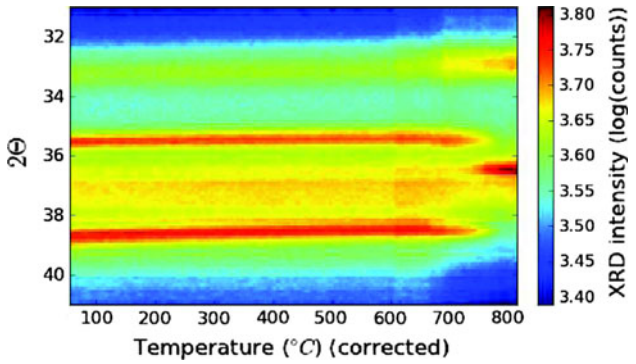

Fig. 6 Variation of XRD intensities with corrected temperature during an in situ He-TPR experiment at 15 °C/min heating rate over $CuO–CeO_2/Al_2O_3$

from Cu_2O, namely its (200) diffraction. Hence, high temperature in inert atmosphere can indeed provide enough thermal energy to release oxygen from the oxide and as such reduce the metal. No trace of Cu(111) at 43.2° is found in this experiment.

Table 1 gathers the onset temperatures for the different reduction treatments on $CuO–CeO_2/Al_2O_3$ with the phase transition occurring. Compared to H_2- and C_3H_8-TPR, the temperature of appearance of reduced Cu_2O during thermal reduction lies considerably higher. Compared to the general equation of reduction (4), thermal reduction can be expressed as a sequential process:

Table 1 Onset temperatures and phase transition occurring during H_2-, C_3H_8- and He-temperature programmed reduction of $CuO–CeO_2/Al_2O_3$, determined from in situ XRD measurements

Catalyst	TPR atmosphere	Onset temperature (°C)	Process
$CuO–CeO_2/Al_2O_3$	H_2	250	$CuO \rightarrow Cu$
	C_3H_8	400/427	$CuO \rightarrow Cu_2O \rightarrow Cu$
	He	727	$CuO \rightarrow Cu_2O$

$$4CuO \leftrightarrow 2Cu_2O + O_2 \quad (5)$$

$$2Cu_2O \leftrightarrow 2Cu + O_2 \quad (6)$$

Although the onset temperature for thermal reduction from CuO to Cu_2O lies quite high, the thermal process of loosening the oxygen bonds will start before the oxygen is actually lost to the atmosphere, i.e. below the temperature of appearance of Cu_2O. Hence, in any reaction at elevated temperature, the mere process of heating will provide more weakly bound oxygen species at the surface, which are easier to react with.

The CeO_2(200) peak position as a function of temperature shows an enhanced downward shift from T = 557 °C onward, consistent with a partial thermal reduction in addition to thermal lattice expansion (see Fig. 7).

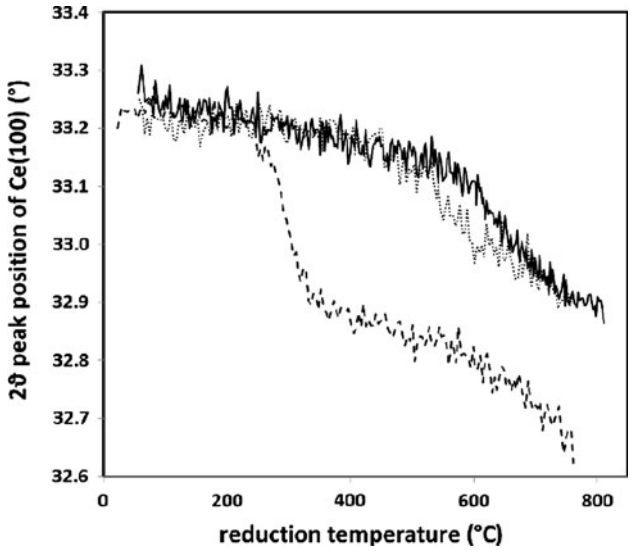

Fig. 7 CeO_2(200) peak position for CuO–CeO_2/Al_2O_3 as a function of temperature for different temperature programmed reductions; *solid line*: He-TPR, *dotted line*: C_3H_8-TPR, *dashed line*: H_2-TPR

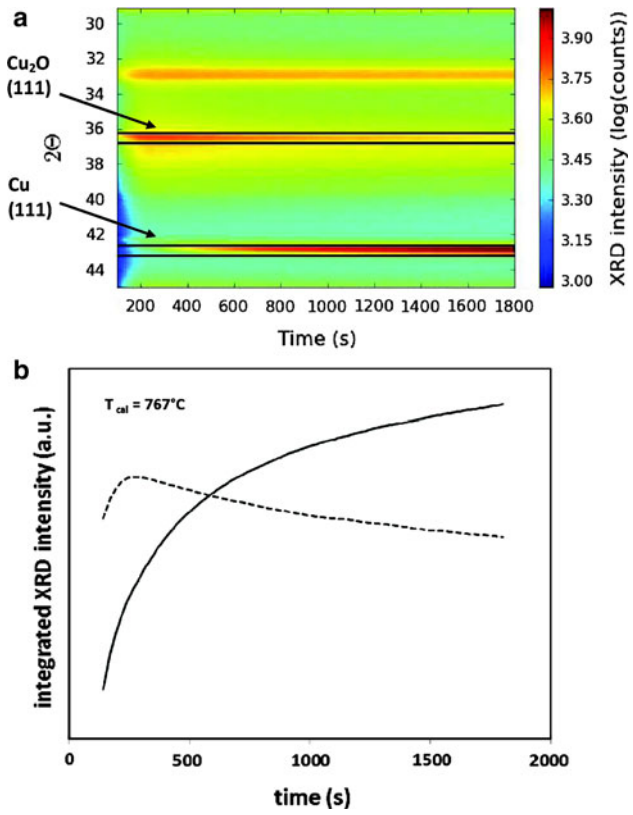

Fig. 8 In situ XRD experiment during isothermal reduction in He at 767 °C, reached by fast heating (300 °C/min); **a** XRD intensities versus time; **b** averaged integrated intensities of Cu_2O(111) (*dashed line*) and Cu(111) (*solid line*) diffraction peaks as a function of time; the integration zones are marked in **a**

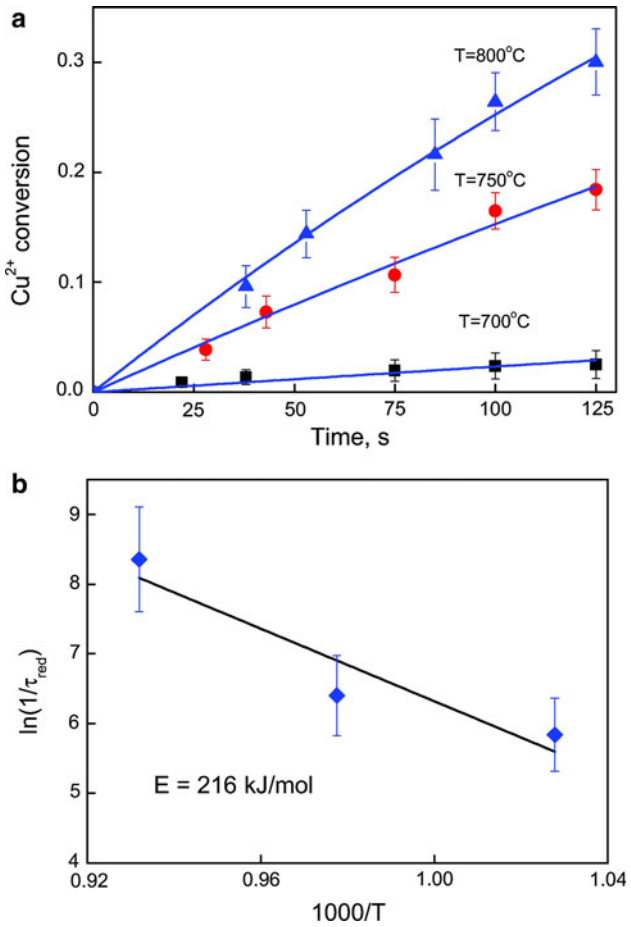

Fig. 9 **a** Conversion of CuO during the thermal reduction of the CuO–CeO_2/Al_2O_3 at different temperatures; the *lines* are calculated according to Eq. (7). **b** Arrhenius relation for catalyst thermal reduction; activation energies are reported with their individual ~95 % confidence intervals

Comparing the shift in CeO_2(200) peak position induced by thermal reduction to the one caused by C_3H_8 reduction, only a slight difference in onset is observed (Fig. 7). Hence, the addition of propane to the gas atmosphere adds only in a limited way to the CeO_2 reduction and the main part is caused by the thermal process of losing oxygen. In H_2-TPR however, the influence of the reactive gas is clearly noticeable as the downward shift of CeO_2(200) position occurs at far lower temperature than for thermal or C_3H_8 reduction (Fig. 7). So, not only CuO but also CeO_2 is subject to thermal reduction. According to the Ellingham diagram for the reduction of CeO_2 to Ce_2O_3, the equilibrium O_2 partial pressure at 800 °C is 10^{-13} bar. Hence, from a thermochemical viewpoint unsupported CeO_2 is stable at this temperature. The fact that is does reduce partially upon heating under inert atmosphere as in the present experiments, is indicative of its interaction with CuO.

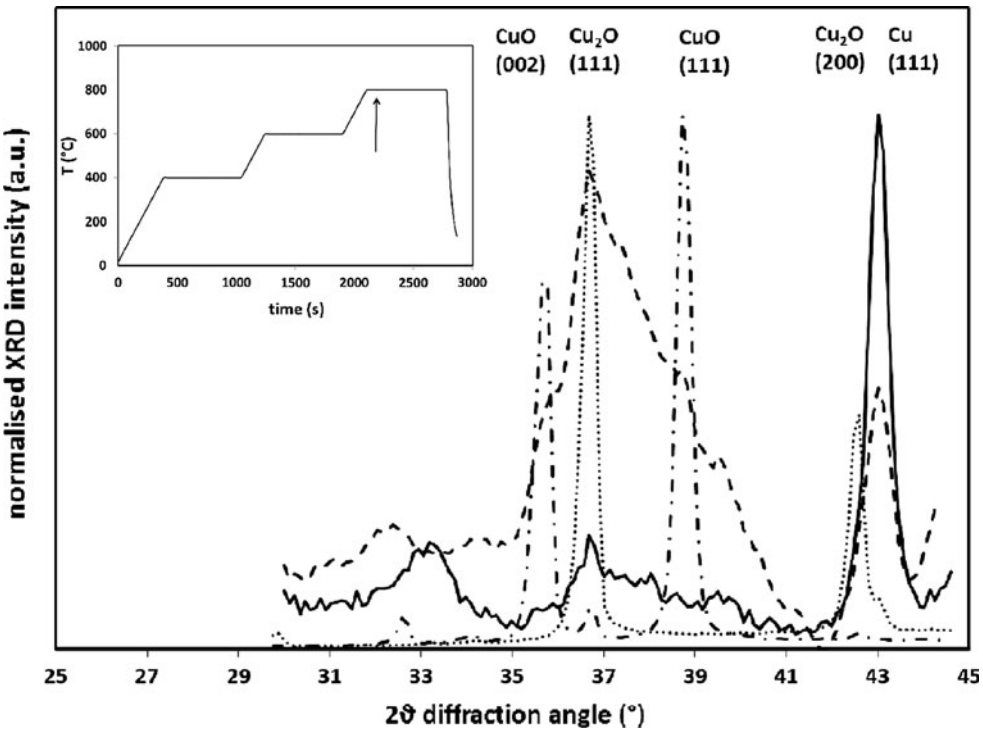

Fig. 10 XRD patterns for CuO (*dash–dotted line*), Cu_2O (*dotted line*), CuO/Al_2O_3 (*dashed line*) and $CuO–CeO_2/Al_2O_3$ (*solid line*) in a stepwise, 400, 600 and 800 °C isothermal reduction experiment under He, recorded 50 s after reaching 800 °C. *Inset*: temperature profile; the *arrow* indicates the (t, T) point of the displayed patterns

Table 2 Programmed stepwise (400–600–800 °C) isothermal reduction in He for supported catalysts CuO/Al_2O_3 and $CuO–CeO_2/Al_2O_3$, and for unsupported CuO and Cu_2O: time of appearance of Cu_2O and Cu

Catalyst	Time of appearance (s)	
	Cu_2O	Cu
CuO	2,100	–
CuO/Al_2O_3	2,100	2,100
$CuO–CeO_2/Al_2O_3$	1,450	1,600

Isothermal reduction of $CuO–CeO_2/Al_2O_3$ under He flow is performed at 700, 750 and 800 °C (767 °C calibrated), by fast ramping to the reduction temperature, each time with fresh catalyst material. The dissociation of CuO starts at temperature 700 °C with the appearance of Cu_2O after 750 s at this temperature and the slow, continuous decrease in intensity of CuO peaks (not shown). For isothermal reduction at 750 °C, Cu_2O appears shortly after the start of the experiment. CuO disappears gradually, leaving Cu_2O as the only remaining phase (not shown). Finally at 800 °C, CuO diffractions disappear rapidly, while Cu2O appears simultaneously and remains present until the end of the experiment. Its intensity reaches a maximum around 250 s after the heating started. Crystalline Cu is formed from t = 100 s on and displays a continuous increase in intensity with time, see Fig. 8.

For each of the isothermal reduction temperatures 700, 750 and 800 °C, the peak position of the $CeO_2(200)$ diffraction hardly varies (not shown). However, the higher the temperature, the lower the average peak position is, indicating that the lattice parameter for CeO_2 is increased when going to a higher temperature. This is in agreement with the variation in peak position during thermal reduction (Fig. 7), since the temperatures of isothermal reduction lie within the temperature range where reduction of CeO_2 occurs in addition to thermal lattice expansion.

To obtain an estimate of the rate of reduction, characteristic time constants for CuO thermal reduction τ_{red} have been calculated assuming a first order approximation:

$$X_{Cu2+} = 1 - e^{-t/\tau red} \quad (7)$$

In order not to include reduction of Cu_2O to Cu in the estimated rate of surface reduction, only the data obtained during the first 125 s as shown in Fig. 9a have been modelled using Eq. (7). The time constants for catalyst reduction were 344, 603 and 4247 s for reaction temperatures 800, 750 and 700 °C, respectively. The thermal reduction process significantly speeds up at higher temperatures. Presenting the time constants in an Arrhenius diagram (Fig. 9b) allows determining an apparent activation energy of 216 ± 54 kJ/mol for catalyst thermal reduction. This value is considerably higher than the activation energy for reduction of the fully oxidized catalyst by hydrogen or propane, namely 20 and 70 kJ/mol respectively [7, 23]. It is however in line with the value reported for thermal reduction of pure CuO, 190 ± 60 kJ/mol [33].

A programmed stepwise isothermal reduction experiment at 400, 600 and 800 °C in He was performed for supported CuO/Al_2O_3 and $CuO–CeO_2/Al_2O_3$, as well as for unsupported Cu_2O and CuO samples. Figure 10 shows the temperature profile and compares XRD patterns for the four samples recorded 50 s after reaching 800 °C. Unsupported CuO shows CuO diffractions (002) and (111), with a small contribution from Cu_2O at 36.4° and 42.3°. For Cu_2O powder, mainly diffraction peaks of Cu_2O are present, with a faint trace of Cu(111) at 43.2°, evolving as a shoulder to the $Cu_2O(200)$ diffraction. This matches the findings of Kirsch and Ekerdt [34] who reported that thin CuO and Cu_2O films reduced thermally from 617, resp. 800 °C on. Hence, after 50 s at 800 °C as in the present XRD experiments, CuO has started to reduce to Cu_2O, while Cu_2O is still largely unreduced. Supported but unpromoted CuO/Al_2O_3 shows weak contributions of both CuO and Cu_2O diffractions, superimposed upon the broad $Al_2O_3(311)$ peak at 37.5°, and a strong Cu metal phase. $CuO–CeO_2/Al_2O_3$ on the other hand has in addition to the Al_2O_3 peak a faint $Cu_2O(111)$ diffraction but mainly a dominant Cu(111) phase. Based on the complete stepwise programmed experiment, the time of appearance of the reduced copper phases was determined for all CuO samples (Table 2). In CuO, Cu_2O only appears after 2100 s of heating, when the temperature is already at 800 °C and there is no sign of Cu. For CuO/Al_2O_3, both Cu_2O and Cu appear after 2100 s, i.e. at 800 °C. In $CuO–CeO_2/Al_2O_3$, these two reduced phases start evolving from 1,450 to 1,600 s on, respectively.

From the comparison of the different CuO samples in Table 2 and Fig. 10, it follows that the support influences the thermal reduction of CuO in He and determines the level of reduction that is reached for a specific sample and temperature. For a similar thermal treatment in He, CuO is partly reduced to Cu_2O, while CuO/Al_2O_3 is able to reach a mix of CuO, Cu_2O and Cu phases. Despite the smaller crystallite size of unsupported CuO compared to the supported CuO/Al_2O_3, the reduction of the latter proceeds further than for the former, indicating that the support ensures the enhancing effect at high temperature. After the thermal treatment, the unsupported materials have clearly suffered from sintering as their crystallite size has grown to about 55 nm. This reduces their BET value accordingly (to $\sim$20 m^2/g). For the supported catalyst, the crystallite size and BET value remain the same.

If CeO_2 is added to promote the CuO activity, $CuO–CeO_2/Al_2O_3$ is reduced faster than CuO/Al_2O_3. This is in agreement with previous work where it was found that Cu-doped ceria has better redox properties than pure CuO [6, 35, 36]. Likewise, the activity of $CuO–CeO_2/Al_2O_3$ in propane oxidation has been found to exceed the one of CuO/Al_2O_3 [6, 12]. The interaction between CeO_2 and CuO has been reported before to be the reason for the enhanced activity of $CuO–CeO_2/Al_2O_3$ catalysts [6, 35, 36].

4 Conclusions

The structure of $CuO–CeO_2/Al_2O_3$, CuO/Al_2O_3 and unsupported CuO and Cu_2O catalysts is investigated under H_2, C_3H_8 and thermal reducing conditions, using time-resolved in situ X-ray diffraction.

Supported and promoted $CuO–CeO_2/Al_2O_3$ undergoes in H_2-TPR a direct transition to metal Cu around 257 °C. At the same temperature, a partial reduction of CeO_2 is noted as a lattice size increase superimposed upon the thermal expansion, although the reduced Ce_2O_3 phase is not reached. Under C_3H_8-TPR, a two-step reduction $CuO \rightarrow Cu_2O \rightarrow Cu$ is observed, while CeO_2 is again reduced partly around 447 °C, i.e. when Cu_2O is formed.

Isothermal reduction experiments in He show that supported CuO, as in $CuO–CeO_2/Al_2O_3$ or CuO/Al_2O_3, is more easily reduced by thermal treatment than bulk CuO and Cu_2O. The addition of CeO_2 as promoter to the $CuO–CeO_2/Al_2O_3$ catalyst facilitates reduction of the supported CuO phase, compared to CuO/Al_2O_3. Supported CuO in $CuO–CeO_2/Al_2O_3$ is mainly reduced to Cu at 800 °C under He and this thermal reduction requires an apparent activation energy of 216 ± 54 kJ/mol.

Heating of $CuO–CeO_2/Al_2O_3$ in inert atmosphere also induces reduction for both CuO and CeO_2, albeit at higher temperature. CuO starts reducing at 727 °C, while CeO_2 is reduced from 557 °C on. This indicates that thermal energy can provide weakly bound oxygen atoms at the catalyst surface, which are very reactive for oxidation reactions.

Acknowledgments This work was supported by the 'Long Term Structural Methusalem Funding by the Flemish Government'.

References

1. Armor JN (1992) Appl Catal B 1:221–256
2. Everaert K, Baeyens J (2004) J Hazard Mater 109:113–139
3. Christopher JGI, Heyes J, Hilary J, Moss JARL (1982) J Chem Technol Biotechnol 32:1025–1033
4. Larsson P-O, Andersson A (1998) J Catal 179:72–89
5. Wang C-H, Lin S-S, Chen C-L, Weng H-S (2006) Chemosphere 64:503–509
6. Heynderickx PM, Thybaut JW, Poelman H, Poelman D, Marin GB (2010) J Catal 272:109–120
7. Alexopoulos K, Anilkumar M, Reyniers M-F, Poelman H, Cristol S, Balcaen V, Heynderickx PM, Poelman D, Marin GB (2010) Appl Catal B 97:381–388
8. Huang T-J, Tsai D-H (2003) Catal Lett 87:173–178
9. Doornkamp C, Ponec V (2000) J Mol Catal A 162:19–32
10. Grzybowska-Świerkosz B (2000) Top Catal 11–12:23–42
11. Busca G, Daturi M, Finocchio E, Lorenzelli V, Ramis G, Willey RJ (1997) Catal Today 33:239–249

12. Balcaen V, Roelant R, Poelman H, Poelman D, Marin GB (2010) Catal Today 157:49–54
13. Rubio O, Herguido J, Menéndez M (2003) Chem Eng Sci 58:4619–4627
14. Haber J, Turek W (2000) J Catal 190:320–326
15. Liu D-J, Robota HJ (1993) Catal Lett 21:291–301
16. Amano F, Tanaka T, Funabiki T (2004) J Mol Catal A 221:89–95
17. Iwamoto M, Yahiro H, Tanda K, Mizuno N, Mine Y, Kagawa S (1991) J Phys Chem 95:3727–3730
18. Llabres i Xamena FX, Fisicaro P, Berlier G, Zecchina A, Palomino GT, Prestipino C, Bordiga S, Giamello E, Lamberti C (2003) J Phys Chem. B 107: 7036–7044
19. Menon U, Galvita VV, Marin GB J Catal. 283:1–9
20. http://www.numpy.org
21. http://www.scipy.org
22. Wang X, Hanson JC, Frenkel AI, Kim J-Y, Rodriguez JA (2004) J Phys Chem B 108:13667–13673
23. Kim JY, Rodriguez JA, Hanson JC, Frenkel AI, Lee PL (2003) J Am Chem Soc 125:10684–10692
24. Kim JY, Hanson JC, Frenkel AI, Lee PL, Rodriguez JA (2004) J Phys Condens Matter 16:S3479–S3484
25. Yamaguchi A, Shido T, Inada Y, Kogure T, Asakura K, Nomura M, Iwasawa Y (2001) Bull Chem Soc Jpn 74:801–808
26. Reitz TL, Lee PL, Czaplewski KF, Lang JC, Popp KE, Kung HH (2001) J Catal 199:193–201
27. Oguchi H, Kanai H, Utani K, Matsumura Y, Imamura S (2005) Appl Cat A 293:64–70
28. Smith ML, Campos A, Spivey JJ (2012) Catal Today 182:60–66
29. Silversmit G, Poelman H, Balcaen V, Heynderickx PM, Olea M, Nikitenko S, Bras W, Smet PF, Poelman D, De Gryse R, Reniers MFO, Marin GB (2009) J Phys Chem Solids 70:1274–1284
30. Aneggi E, Boaro M, de Leitenburg C, Dolcetti G, Trovarelli A (2006) J Alloys Compd 408–412:1096–1102
31. Martinez-Arias A, Gamarra D, Fernandez-Garcia M, Wang XQ, Hanson JC, Rodriguez JA (2006) J Catal 240:1–7
32. Cao Y, Casenas B, Pan W-P (2006) Energy Fuels 20:1845–1854
33. Malinin GV, Tolmachev YM (1975) Russ Chem Rev 44:392
34. Kirsch PD, Ekerdt JG (2001) J Appl Phys 90:4256
35. Bera P, Aruna ST, Patil KC, Hegde MS (1999) J Catal 186:36–44
36. Shapovalov V, Metiu H (2007) J Catal 245:205–214